Mon. Not. R. Astron. Soc. **000**, 000–000 (0000) Printed 16 January 2017 (MN LATEX style file v2.2)

Numerical study of $N = 4$ binary-binary scatterings in a background potential

Taeho Ryu[1⋆], Nathan W. C. Leigh[2], Rosalba Perna[1]
[1]*Department of Physics and Astronomy, Stony Brook University, Stony Brook, NY 11794-3800, USA*
[2]*Department of Astrophysics, American Museum of Natural History, Central Park West and 79th Street, New York, NY 10024*

16 January 2017

arXiv:1611.09358v2 [astro-ph.SR] 13 Jan 2017

ABSTRACT

We perform a large suite of $N = 4$ numerical scattering experiments between two identical binaries consisting of identical point particles in a (continuous) background potential. For investigative purposes, we assume a uniform (natal or star-forming) gas medium. We explore a range of constant gas densities, from $n = 10$ cm^{-3} to 10^5 cm^{-3}. These densities are relevant for various astrophysical environments, including star-forming molecular clouds and denser, fragmented cores within these clouds. Our primary goal is to characterize the effects of the background potential on the subsequent stellar dynamics. We consider the outcome probabilities and the properties of any binaries formed during the binary-binary encounters, such as the distributions of binary binding energies and eccentricities. We also present the final velocity distributions of the ejected single stars.

The background potential has two important effects on the stellar dynamics: 1) The potential acts to reset the zero-point of the total system energy, which affects the types and properties of the products of the encounter; 2) For higher n and weakly bound systems (i.e., large semimajor axes), the stellar dynamics are significantly affected when stars become trapped in the potential, oscillating around the system centre of mass (CM). This, in turn, increases the number of scattering events between stars (single, binary or triple) near the CM and makes it harder for single stars to escape to infinity. This ultimately leads to the preferential ionization of triples and wide binaries and the survival of compact binaries, with the single stars escaping at very high ejection velocities.

Key words: chaos − gravitation − stellar dynamics : background potential − homogeneous medium : scatterings − binaries: general.

1 INTRODUCTION

The N-body problem has been a topic intensively investigated by a number of studies using numerical simulations. There have been enormous achievements in studies of 3-body (e.g Heggie & Hut 1993; Mikkola 1994; Heggie, Hut & McMillan 1996) and 4-body scattering problems (e.g Mikkola 1983, 1984; Leigh et al. 2016) along with increasing computational capability, which render us a more extensive and deeper understanding of the dynamical phenomena occurring over the course of the evolution of stellar clusters. However, our understanding of these processes remains incomplete.

Binary-binary encounters dominate over binary-single encounters in star clusters with binary fractions $\gtrsim 10\%$ (Sigurdsson & Phinney 1993; Leigh & Sills 2011). Hence, binary-binary interactions are particularly important in dense stellar environments with high binary fractions. This is the case ($\gtrsim 30 - 50\%$) in open clusters (e.g Halbwachs et al. 2003; Sana et al. 2008; Sana, Gosset & Evans 2009; Sollima et al. 2010; Sana, James & Gosset 2011; Leigh & Geller 2013) and the solar neighborhood (e.g Abt & Levy 1976; Duquennoy & Mayor 1991; Reid & Gizis 1997; Cool & Bolton 2002). It follows that binary stars can play an important role in the evolution of star clusters with high binary fractions. The binary frequencies in the cores of globular clusters are relatively low ($\lesssim 10\%$, Rubenstein & Bailyn e.g 1997; Albrow et al. e.g 2001; Ji & Bregman e.g 2015), such that binary-single interactions can dominate over binary-binary interactions (Sigurdsson & Phinney 1993; Leigh & Sills 2011). Regardless, it is generally accepted that close encounters between binaries occur commonly in globular clusters (Hills & Day 1976; Hut & Verbunt 1983; Hut 1985). The binary fractions in the cores of clusters tend to be elevated relative to

⋆ email: taeho.ryu@stonybrook.edu

© 0000 RAS

the outskirts due to mass segregation induced by two-body relaxation. Binary-binary encounters should produce triple star systems commonly (e.g. Leigh et al. 2016). Triples can also form via dissipative tidal captures (e.g Bailyn 1989) or scatterings involving pre-existing triples (e.g. Leigh & Sills 2011; Leigh & Geller 2012, 2013; Leigh et al. 2015; Antognini & Thompson 2016).

Dynamical scatterings between binaries provide a formation channel for compact binary systems. In general, hard binaries are hardened further during binary-binary encounters via the slingshot mechanism, while soft binaries are ionized (Heggie 1975; Hills & Day 1976). In this context, of particular interest are the three gravitational wave events recently reported by aLIGO, i.e. GW150914, GW151226 and LVT151012 (The LIGO Scientific Collaboration et al. 2016). These are believed to have originated from the coalescence of two massive black holes in a binary system. Many authors have pointed out that the formation of compact binary black holes via stellar scatterings in dense star clusters is a feasible mechanism for the formation of these binary black holes, and that the measured BH masses are consistent with this formation channel (Portegies Zwart & McMillan 2000; Abbott et al. 2016, and references therein). At high redshifts ($z \sim 15 - 20$), compact (and wider) black hole binaries, such as high mass X-ray binaries, consisting of the first remnants from Population III stars could form via binary-binary interactions in star-forming clouds (Ryu, Tanaka & Perna 2016). Once formed, these black hole binaries could evolve into even more compact binaries (depending on the initial binary orbital parameters), possibly contributing to future GW detections by Advanced LIGO (e.g Belczynski et al. 2016). In addition to hardening binaries, physical collisions (and mergers) could occur when two binaries interact directly (Hills & Day 1976; Fregeau et al. 2004; Leigh & Geller 2012; Leigh et al. 2015). This has been discussed as a viable mechanism for the formation of blue stragglers, observed in both open and globular clusters (Leonard 1989; Davies, Piotto & de Angeli 2004; Leigh, Sills & Knigge 2007; Knigge, Leigh & Sills 2009).

To date, most authors studying small-number scattering interactions have focused on isolated stellar dynamics (analytically and numerically). However, observational evidence suggests that all dense clusters experience a phase where gas and stars co-exist (Brown & Zuckerman 1975; Samson 1975). Here, stars and binaries undergo direct interactions in the presence of a background gas medium. This phase may be a natural consequence of the formation of dense clusters. Briefly, stars form out of cool, dense gas. Eventually, the gas is removed from the cluster, possibly due to stellar winds and/or supernovae explosions. This reduces the binding energy of the cluster, liberating stars from the outskirts in the process. The existence of multiple stellar populations in globular clusters (Gratton, Carretta & Bragaglia 2012, and references therein) suggests that this could have occurred more than once over the cluster life time (Lin & Murray 2007). Therefore, unveiling the stellar dynamics in a background gas medium may be essentially the first step in connecting the gap between the gas-dominated star formation regime and the gas-free stellar dynamics regime.

The goal of this paper is to characterize the effects of a continuous background potential on the time evolution of binary-binary interactions. To this end, we present the results of a large suite of numerical N-body simulations of binary-binary scatterings in a background potential. For simplicity, we model the background potential as an uniform (natal or star-forming) gas medium. *We consider only the gravitational effects of the background potential,* and ignore any gas damping effects (dynamical friction, accretion, etc.). Hence, our choice for the gas density directly determines the total mass of the potential for a given outer boundary, or, equivalently, it determines the location of the outer boundary for a given total gas mass. We consider a range of (discrete) constant gas densities, from $n = 10$ cm^{-3} to 10^5 cm^{-3}. These densities are typical for molecular clouds (i.e. regions of star formation)

We primarily focus on the outcome probabilities and the properties of any binaries formed during the encounters. We find that one of the important roles of the background potential (for any non-zero number density) is to reset the zero-point of the total system energy. This in turn affects the types of objects formed during the encounters in addition to the outcome probabilities. In particular, for higher n and less tightly bound systems (i.e., larger semimajor axes), stars often become trapped in the background potential, oscillating with a short period around the system center of mass. This results in fewer triples and wider binaries and the preferential survival of compact binaries, since subsequent scatterings continue until two single stars escape at very high ejection velocities. Note that we only consider the gravitational influence of the background potential and do not consider gas dynamical friction, gas damping or gas accretion. We emphasize that our results are general to any continuous background potential (e.g., dark matter), and are not just limited to a constant gas medium. Hence, we shall use throughout this paper "continuous background potential" instead of gravitational gas potential.

The paper is organized as follows. We start in §2 by describing the implementation of the background potential in our scattering code, including the code termination criteria and our choices for the initial conditions. We present our results in §3, including the outcome probabilities and the properties of any binaries formed during the interactions. Finally, we summarize the effects of the background potential on the stellar dynamics in our simulations, and discuss the implications of our work for real astrophysical environments in §4.

2 METHOD

In this section, we provide descriptions of the numerical scattering simulations of binary-binary encounters, the background gas medium and the termination criteria adopted for the simulations.

2.1 Overview of the scattering experiment

We investigate the products of binary-binary encounters in a continuous background potential. The equations of motion of four stars are solved with the 4th - order & 5 - stage Runge-Kutta-Fehlberg method (Erwin 1969) using adaptive time steps. The numerical method is a very precise and stable integration method among the large class of Runge-Kutta schemes, particularly by adopting the Butcher

tableau for Fehlberg's 4(5) method. To ensure numerical precision, given the initial total energy of the system E_0, the numerical error in the total energy of the system ($|(E(t) - E_0)/E_0|$) where $E(t)$ is defined in the equation 8) never exceeds $10^{-4} - 10^{-6}$ in all simulations. This is achieved by varying the value of each subsequent time step with the error control tolerance of 10^{-10}. In order to maintain an acceptable computation speed throughout the simulations, we additionally set a minimum value for the time step, $10^{-7} \times \tau_{\rm dyn,\,min}$, where $\tau_{\rm dyn,\,min}$ is the smallest value of the dynamical time between any two stars in the simulation at a given time step.

We perform 10^3 scattering experiments of two identical binaries with the same initial semimajor axis for every given set of simulations. The number of simulations for each set is sufficiently large to ensure that all data statistically converge (the overall Poisson uncertainties $\lesssim 3 - 4\%$). In total, we consider three discrete values of the semimajor axis ($a_0 = 1$ AU, 10 AU and 100 AU). We first generate two identical binaries with initially circular orbits (the eccentricities are zero, or $e = 0$). Each binary consists of two point particles, each with a mass of 1 $M_\odot$. Then we give an initial separation and relative velocity between the centre of mass of the two binaries, such that they collide head-on at the origin (i.e., with impact parameter $b = 0$) with nearly zero total energy (more precisely, slightly negative to positive depending on the number density of the gas medium, but we defer a more detailed explanation of this to section 2.2). However, the mutual inclinations between the binary orbital planes, as well as their initial phases, are randomly chosen.

In order to choose the value of the initial relative velocity $v_{\rm rel}$ between the centres of mass of the two binaries, we define the critical velocity $v_{\rm cri}$ as the relative velocity between the centres of mass of the two binaries at infinity for which the total encounter energy is zero. In this paper, $v_{\rm rel}$ will be presented in units of $v_{\rm cri}$, unless otherwise stated. More explicitly, in the case of binary-binary encounters, the total initial energy E_0 at infinity is written as follows:

$$E_0 = \frac{1}{2}\mu v_{\rm rel}^2 - \frac{Gm_{11}m_{12}}{2a_1} - \frac{Gm_{21}m_{22}}{2a_2}\,, \tag{1}$$

In this equation, the first subscript for the particles mass m, along with the binary semimajor axis a subscript, corresponds to each binary, whereas the second subscript for m corresponds to each component of the binary. For example, the masses of the two stars in the $1_{\rm st}$ binary with semimajor axis a_1 are m_{11} and m_{12}. Here, μ in the first term on the right hand side is the reduced mass of the two binaries, i.e., $\mu = (m_{11} + m_{12})(m_{21} + m_{22})/(m_{11} + m_{12} + m_{21} + m_{22}) = 1$ $M_\odot$. The second and third terms are the orbital energies of the two binaries. Note that the gravitational potential between the two binaries is zero at infinity. Therefore, the critical velocity at $E_0 = 0$ is,

$$v_{\rm cri} = v_{\rm rel}(E_0 = 0) = \sqrt{\frac{2}{\mu}\Big(\frac{Gm_{11}m_{12}}{2a_1} + \frac{Gm_{21}m_{22}}{2a_2}\Big)}, \tag{2}$$

In this study, we take $v_{\rm rel} = 1$ to explore the zero-energy limit.

In the presence of a background gas medium, the condition $v_{\rm rel} = 1$ does not necessarily imply that the total encounter energy is exactly zero. Instead, we achieve the zero-energy limit by adjusting the initial separations between the binary centers of mass. In order to explain how we determine the initial distance between the two binaries, we first need to introduce the background potential adopted in this study, corresponding to a constant density gas medium.

2.2 Background gravitational potential

In this section, we describe the background gravitational potential adopted in our experiments, the choice of initial conditions, and the resulting motions of the stars.

We assume a uniform (i.e. constant) density ρ (n is the gas number density) for this potential, with a limiting outer boundary $r_{\rm bg}$ set by our chosen total background mass $M_{\rm gas}$ such that

$$\rho = \begin{cases} nm_{\rm H} & r \leqslant r_{\rm bg}; \\ 0 & r > r_{\rm bg}. \end{cases} \tag{3}$$

where $m_{\rm H}$ is the mass of a hydrogen atom. For simplicity, we take a mean molecular weight of unity. The mass of gas enclosed in a spherical volume of radius r can be written as

$$M_{\rm en,gas}(r) = \begin{cases} \frac{4\pi}{3}\rho r^3 & r \leqslant r_{\rm bg}; \\ \frac{4\pi}{3}\rho r_{\rm bg}^3 = M_{\rm gas} & r > r_{\rm bg}. \end{cases} \tag{4}$$

We consider a range of densities, motivated by the values typical of gaseous astrophysical environments, most notably giant molecular clouds and star-forming regions. In this case, the gravitational force imparted by a uniform gas medium of constant density on a given star particle at r follows the analytic formula:

$$\mathbf{f}_{\rm bg}(r) = -\frac{GmM_{\rm en,gas}(r)}{r^3}\mathbf{r} \tag{5}$$

$$= \begin{cases} -\frac{4}{3}\pi Gm\rho\,\mathbf{r} & r \leqslant r_{\rm bg}; \\ -\frac{4}{3}\pi Gm\rho\Big(\frac{r_{\rm bg}}{r}\Big)^3\mathbf{r} & r > r_{\rm bg}. \end{cases} \tag{6}$$

where m is the mass of the star and $\mathbf{r}$ is the vector pointing from the system CM to the star. Accordingly, the background potential has the following form:

$$V_{\rm bg}(r) = \begin{cases} \frac{2}{3}\pi Gm\rho r^2 & r \leqslant r_{\rm bg}; \\ -\frac{GmM_{\rm gas}}{r} = -\frac{4}{3}\pi Gm\rho\frac{r_{\rm bg}^3}{r} & r > r_{\rm bg}. \end{cases} \tag{7}$$

And the total energy $E(t)$ of four stars in the system at t, including the contribution from $V_{\rm bg}(r)$, can be written as,

$$E(t) = \sum_{i=1}^{4}\frac{1}{2}m_i v_i^2 - \sum_{\substack{i,j=1 \\ (i>j)}}^{4}\frac{Gm_i m_j}{|\mathbf{r}_i - \mathbf{r}_j|} + \sum_{i=1}^{4}V_{\rm bg}(r_i) \tag{8}$$

where m_i is the mass of each star and v_i is the velocity of each star with respect to the system CM.

Note that we consider only the gravitational force imparted by the background potential, and ignore any dissipative effects caused by the motions of macroscopic objects in a dense gaseous medium. The background potential is assumed to remain static in time. There is also no stellar mass growth via gas accretion or dissipative effects due to the gas.

In general, the background potential provides additional

gravitational forces that accelerate the stars initially, increasing the relative velocity at impact. When the stars approach the system CM at the moment of impact, the influence of the background potential becomes (instantaneously) small. On the other hand, when the star particles are moving away from each other after scattering events or ejections, the potential may play an important role as an inward restoring force. This ultimately prevents or delays dissociation, and increases the probability of subsequent encounters (depending on the gas density).

Taking the background potential into account, the initial total energy for the two binaries (1 and 2) located at initial distances r_1 and r_2 from the system CM (their initial separation is r_{12}) becomes:

$$\begin{aligned} E_0 &= \frac{1}{2}\mu v_{\rm rel}^2 - \frac{Gm_{11}m_{12}}{2a_1} - \frac{Gm_{21}m_{22}}{2a_2} \\ &+ \frac{2}{3}\pi G m_1 \rho r_1^2 + \frac{2}{3}\pi G m_2 \rho r_2^2 - \frac{Gm_1 m_2}{r_{12}} \\ &= \frac{1}{2}\mu v_{\rm rel}^2 - 2\frac{Gm_{11}m_{12}}{2a_1} + \frac{4}{3}\pi G m_1 \rho \left(\frac{r_{12}}{2}\right)^2 - \frac{Gm_1 m_2}{r_{12}}. \end{aligned} \quad (9)$$

In the second equality, we simplified the equation using the fact that the two binaries are identical and the CM of the two binaries coincides with the origin initially, i.e. $r_1 = r_2 = r_{12}/2$. Here, the gravitational potential energy (the last term) should not be ignored because the two binaries are initially separated by a finite distance in our simulations. Since we take $v_{\rm rel} = 1$, the first two terms always cancel out, regardless of a_1 (and $a_2 = a_1$). Hence, in the limit of $E_0 = 0$, r_{12} is determined by the requirement that the last two terms cancel each other.

In our experiments, we fix r_{12} such that $E_0 = 0$ when $n = 10^2$ cm^{-3}. In order to explore the effects of the background potential, we run suites of simulations with a range of densities, i.e., $n = 10, 10^2, 10^3$ and 10^5 cm^{-3} (default set). For this defualt set, we take $M_{\rm gas} = 10^{10}$ M$_\odot$ so that the width of the potential ($r_{\rm bg}$) is large enough for all particles to remain within the spherical volume defined by this critical radius throughout the duration of the interaction ($r_{\rm bg}$ for the chosen total gas mass is depicted in Figure 2). For comparison, we run additional simulations with even higher number densities and larger semimajor axes. As we will show, the background potential resets the zero-point of the total system energy. In particular, the stellar dynamics are significantly affected by the background potential when the stars become trapped in the potential, oscillating with a short period around the system CM. This leads to repeated scattering events that would not otherwise occur without the influence of the background potential.

2.3 Modified termination criteria

Our primary interest in this paper is in the outcome probabilities for binary-binary scatterings. Hence, it is critical to properly define when the interactions between star particles are complete. The simulations terminate when no further scatterings will occur. To begin, we use the same criteria as described in Fregeau et al. (2004). These criteria consist of four conditions: 1) All single stars and bound hierarchies in a system are moving away from one another. 2) The total energy of the single stars and bound hierarchies are positive (without including the orbital energies of any bound hierarchies). 3) Hierarchies such as triples are dynamically stable. Finally, 4) the relative force between stars in a bound system should be larger at apocenter than the tidal force from all other stars (i.e., bound hierarchies as a whole, if formed) by a certain fraction, the so called tidal tolerance parameter δ. The relative force $F_{\rm rel}$ and the tidal force $F_{{\rm tid},\star}$ on the $i_{\rm th}$ binary at apocenter are:

$$F_{\rm rel} = \frac{Gm_{i1}m_{i2}}{[a(1+e)]^2} \quad (10)$$

$$F_{{\rm tid},\star} = \sum_j \frac{2Gm_i m_j}{r_{ij}^3} a(1+e). \quad (11)$$

Hence, the condition for the tidal tolerance parameter can be written:

$$\frac{F_{{\rm tid},\star}}{F_{\rm rel}} < \delta. \quad (12)$$

We take $\delta = 10^{-9}$, which is a value small enough to allow us to precisely classify the outcomes and explore the effects of the background potential at large distances. For more details, see Fregeau et al. (2004). Additional termination criteria beyond those implemented in Fregeau et al. (2004) are needed in our case. That is, in order to implement physically motivated termination criteria appropriate for scatterings occurring in the presence of a background potential, we must include additional criteria due to the tidal force and the relative force from the *gas*. We calculate them at apocenter as follows:

$$F_{\rm tid,bg} = \frac{4\pi\rho}{3} G m_i [a(1+e)] \quad (13)$$

$$F_{\rm rel} = \frac{Gm_i m_j}{[a(1+e)]^2} \left| 1 - \left(\frac{\frac{4\pi\rho}{3}[a(1+e)]^3}{m_j} \right) \left(\frac{r_i}{a(1+e)} \right) \right| \quad (14)$$

We only consider the minimum relative force for a more strict termination criteria. We then impose two last additional termination criteria, namely a correction to the previous calculation of the tidal tolerance parameter and an additional escape criterion:

5) $\frac{F_{{\rm tid},\star} + F_{\rm tid,bg}}{F_{\rm rel}} < \delta$,

6) $v_i > v_{\rm esc} = \sqrt{\frac{2GM_{\rm en,gas}(r)}{r}}$, where $v_{\rm esc}$ is the velocity requited by a star at r to escape from the gas medium to spatial infinity. Since $v_{\rm esc}$ increases until the star is completely ejected from the background potential well (i.e., at $r > r_{\rm bg}$), the code keeps checking the escape criteria at every time step.

It is possible that an ejected star turns around before escaping to a vacuum region if the instantaneous ejection velocity is not larger than the escape velocity of the whole system. Here, it will simply orbit the CM of the gas medium with a chance of undergoing additional scatterings with other stars. In this case, condition 5) would not be satisfied regardless of all the other conditions. In order to avoid excessively long integration times, we stop the simulations when $t > 10^7 - 10^8$ yr (i.e., the typical life time of a star cluster, Subramaniam et al. 1995) or the distance from the CM of any ejected star exceeds $10^6 - 10^7$ AU.

This additional distance condition can be justified as follows. (a) In our simulations, the gravitational force (or

potential) from the gas dominates at $r > 10^5$ AU when $n = 10^2$ cm^{-3}, compared to the gravitational force from the other stars in the system. (*b*) Given that the tidal radius of a typical star cluster in the Milky Way is < 35 pc (Heggie & Hut 2003), the ejected stars will eventually escape from their host cluster. (*c*) The stellar density in the central region of a typical star cluster is $n = 10^2 - 10^3$ pc^{-3}, so that it is very likely that in such systems the ejected stars will encounter other stars in the cluster before moving a distance of $10^6 - 10^7$ AU (the typical distance between stars is $\sim 10^4 - 10^5$ AU). (*d*) The peak separation between clusters in our Galaxy is $10^5 - 10^6$ AU (Subramaniam et al. 1995).

3 RESULTS

In this section, we present the results of our scattering experiments between two binaries in a background potential including the outcome probabilities and the statistical properties of the final binary and single stars.

3.1 Characterizing the effect of the background potential in different regions

We expect the dynamics of the stars to depend on what the dominant potential is in the region of interaction. In general, as stars approach the system CM, the gravitational forces imparted by the gas become very small ($a_{\rm bg} \sim r$), since the enclosed mass drops to zero. In other words, in the inner region characterized by a distance at which the enclosed mass of gas is the same as the stellar mass ($M_\star$), the stellar dynamics are primarily determined by their mutual gravitational forces. Here, we denote this characteristic distance by $r_\star$, estimated as:

$$\frac{r_\star}{\rm AU} = \Big(\frac{M_\star}{4\pi\rho/3}\Big)^{1/3} \simeq 1.4\times10^5\Big(\frac{M_\star}{3\ {\rm M}_\odot}\Big)^{1/3}\Big(\frac{n}{10^2\ {\rm cm}^{-3}}\Big)^{-1/3} \quad (15)$$

and refer to the inner region bounded by $r_\star$ as *region 1*.

On the other hand, stars outside *region 1* are more heavily influenced by the background potential. Provided the same functional form for the potential (see equation 7) is adopted as for classic simple harmonic motion, stars can become trapped in the background potential, oscillating around the CM with a period of $\sqrt{\frac{3}{4\pi G\rho}}$ and an amplitude of $\sqrt{\frac{3}{4\pi G\rho}}v$ (most likely the instantaneous ejection velocity for v). The amplitude corresponds to the maximum distance reached by the stars, at which point the stars turn around and return toward the system CM. We denote this return distance by $r_{\rm return} = \sqrt{\frac{3}{4\pi G\rho}}v$, and refer to the region enclosed by $r_{\rm return}$ outside *region 1* as *region 2*. The remaining volume ($r_{\rm return} < r \leqslant r_{\rm bg}$) is denoted *region 3*[1]. But in our simulations that the distance is relatively small compared to $\sqrt{\frac{3}{4\pi G\rho}}v$. Figure 1 schematically illustrates the three regions. The blue solid, black dotted and black dashed lines correspond to *region 1*, *region 2* and *region 3*, respectively.

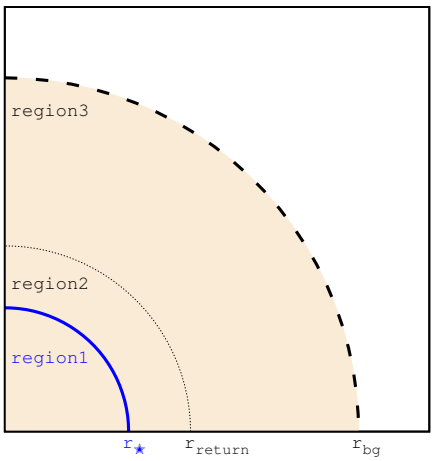

Figure 1. A schematic diagram projected on to the 2-D $x-y$ plane showing the three regions defined by the three characteristic distances, namely $r_\star$, $r_{\rm return}$ and $r_{\rm bg}$. In the inner-most region (blue solid circle) bounded by $r_\star$, the enclosed gas mass $M_{\rm en,gas}$ is smaller than the total stellar mass $M_\star$. $r_{\rm return}$ (black dotted line) indicates the distance at which the stars return towards the system CM, and $r_{\rm bg}$ corresponds to the outer boundary of the gas cloud or potential well.

In our simulations, the typical final separations between stars in a given simulation are determined by the termination criteria (see equation 12), which we call $r_{\rm term}$. This distance $r_{\rm term}$ roughly corresponds to the maximum attainable distance by the ejected stars in our simulations. To see this, note that upon inserting equations 10 and 11 into equation 12, we find:

$$\delta = \frac{F_{\rm tid}}{F_{\rm rel}} \simeq \frac{2G(m_{i1}+m_{i2})m_j}{r_{ij}^3}a(1+e)\frac{[a(1+e)]^2}{Gm_{i1}m_{i2}}$$
$$\simeq (2-40)\Big(\frac{a}{r}\Big)^3\,, \quad (16)$$

where the factor in front accounts for the possible range in eccentricity e and mass ratio q for any combination of bound/unbound systems ($1 \leqslant (1+e)^3 \leqslant 8$ and the term with mass $\sim [2-4.5]$) available to the $N=4$ case. Finally, using the adopted value for δ, $r_{\rm term}$ is expressed as follows:

$$r_{\rm term} \simeq a\Big[\frac{\delta}{(2-40)}\Big]^{-1/3} \simeq 2000\ a\,. \quad (17)$$

If $r_{\rm term} \leqslant r_\star$, the outcomes are determined by stellar interactions taking place only in *region 1*. The small tidal tolerance parameter we take ensures that no further scatterings will occur even though the stars are most likely confined to *region 1* until the end of the simulations. If $r_\star < r_{\rm term} \leqslant r_{\rm return}$, the termination criteria are satisfied when the ejected stars reach *region 2*. Stars in *region 2* start to slow down and become trapped in the background potential. It is still possible that the stars return toward the system CM and undergo subsequent encounters prior to their final ejection. If $r_{\rm return} < r_{\rm term} \leqslant r_{\rm bg}$, the ejected stars are completely bound to the background potential, orbiting around the system CM, causing subsequent scatterings with

[1] Note that in order to more precisely estimate the maximum attainable distance by the stars, we may need to add to $\sqrt{\frac{3}{4\pi G\rho}}v$ a radial distance from the system CM when the stars are completely detached from the stellar subsystem (i.e., positive relative energy between an ejected star and the remaining substellar system).

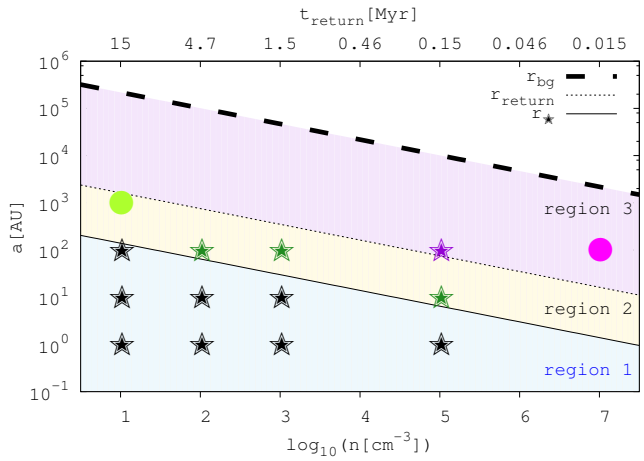

Figure 2. A schematic diagram projected on to the 2-D $n - a_0$ plane showing three distinct regions. The relations between n and a_0 defining the outer boundary of each region are given in Equation 18. We mark all default sets of simulations (stars) as well as two additional sets (solid circles), but with different colors for each region (black for *region1*, green for *region2* and magenta for *region3*). The typical returning times (the oscillation period in yr, $\sqrt{\frac{3}{4\pi G\rho}}$) are indicated along the upper x-axis.

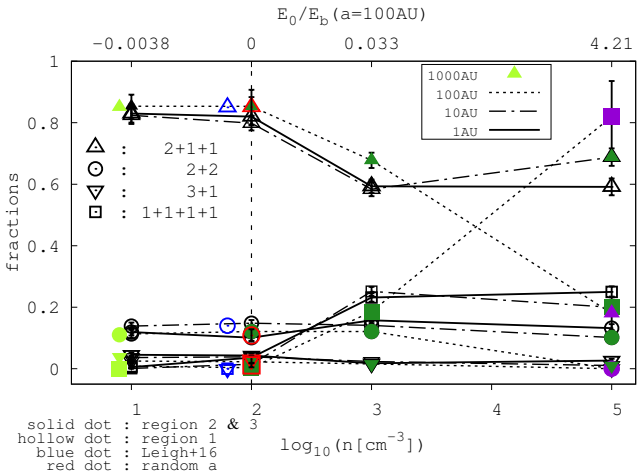

Figure 3. The fraction of each outcome as a function of gas density for three discrete values of the semimajor axs. The different line types correspond to the different semimajor axes: the solid line, dot-dashed line and dotted line represent, respectively, $a_0 = 1$ AU, 10 AU and 100 AU. The different point types indicate the different encounter outcomes: the triangles, circles, down-pointing triangles and square dots correspond to, respetively, the outcomes 2+1+1, 2+2, 3+1 and 1+1+1+1. The outcome fractions at $n = 0$ cm^{-3} and $E_0 = 0$ in Leigh et al. (2016) (see Figure 4 in their paper assuming a virial ratio $k \simeq 1$) are marked as blue dots, and those for our simulations where the semimajor axis is randomly generated in the range of $a_0 = 1 - 100$ AU are marked as red dots. The bright green dots near $n = 10$ cm^{-3} represent the fractions for an additional experiment with $n = 10$ cm^{-3} and $a_0 = 1000$ AU. The setup details are described in the text.

existing binaries or triples left relatively close to the system CM. Assuming the semimajor axis of the final binary is comparable to the initial semimajor axis and $v \sim (1-2)v_{\rm cri}$ (or, roughly the escape velocity from two or three identical point masses), which is indeed what we see in Figures 4 and 6, we can find expressions for $r_\star$, $r_{\rm return}$ and $r_{\rm bg}$ in terms of a_0 and n. That is:

$$\begin{cases} \left(\frac{a_0}{1\ {\rm AU}}\right)\left(\frac{n}{10^2\ {\rm cm^{-3}}}\right)^{1/3} < 10^2 & \textit{region 1}; \\ 10^2 < \left(\frac{a_0}{1\ {\rm AU}}\right)\left(\frac{n}{10^2\ {\rm cm^{-3}}}\right)^{1/3} < 10^3 & \textit{region 2}; \\ 10^3 < \left(\frac{a_0}{1\ {\rm AU}}\right)\left(\frac{n}{10^2\ {\rm cm^{-3}}}\right)^{1/3} < 10^5\left(\frac{M_{\rm gas}}{10^{10}\ {\rm M_\odot}}\right)^{1/3} & \textit{region 3}. \end{cases} \quad (18)$$

Figure 2 shows the three regions in the $n - a_0$ plane based on the relations derived above. We also mark all default sets of simulations (stars) as well as two additional sets (solid circles), but with different colors for each region (black for *region 1*, green for *region 2* and magenta for *region 3*). The typical returning times (the oscillation period in yr, $\sqrt{\frac{3}{4\pi G\rho}}$) are indicated along the upper x-axis.

3.2 Outcome probabilities

We classify the final end products of binary-binary scatterings according to the four outcomes:

(i) a binary and two single stars (2+1+1)
(ii) two binaries (2+2)
(iii) a triple and a single star (3+1)
(iv) four single stars (1+1+1+1)

Henceforth, we will refer to each outcome by what is given in the accompanying parentheses.

Figure 3 shows each outcome probability as a function of gas density for each semimajor axis. The error bars indicate the Poisson uncertainties for each simulation set. The line types differentiate between the different semimajor axes: the solid, dot-dashed and dotted lines correspond to, respectively, $a_0 = 1$ AU, 10 AU and 100 AU. The different point types indicate the different outcomes: the triangles, circles, down-pointing triangles and squares correspond to, respectively, 2+1+1, 2+2, 3+1 and 1+1+1+1. For clarity, we use the same color scheme as in Figure 2 for the simulations in each region.

3.2.1 *Exploring the $E_0 = 0$ neighborhood*

Figure 3 shows that the outcome fractions of our numerical study at $n = 10 - 10^2$ cm^{-3} are almost the same as for the equivalent scattering experiments without a background potential (i.e., with $n = 0$). As n increases from $n = 10^2$ cm^{-3} to $n = 10^3$ cm^{-3}, the total energy becomes positive and the 1+1+1+1 outcome begins to appear for all semimajor axes. To ensure that we have correctly calculated the outcome fractions at this critical energy limit, we run two more sets of simulations: 1) Instead of assuming discrete values for the semimajor axes, we generate two binaries with the same semimajor axis, but randomly generated within the range $a_0 = 1$ AU $- 100$ AU. The results of this experiment (marked with red hollow dots at $n = 10^2$ cm^{-3} in the figure) are consistent with those found adopting discrete values for the semimajor axis; 2) we performed experiments with a density between the two critical densities, or $n \simeq 300$ cm^{-3}

($\log[n/\ \mathrm{cm}^{-3}] = 2.5$) for both $a_0 = 1$ AU and 10 AU. As expected, the outcome fractions for $n \simeq 300\ \mathrm{cm}^{-3}$ fall between those for $n = 10^2\ \mathrm{cm}^{-3}$ and $n = 10^3\ \mathrm{cm}^{-3}$ in all cases. We do not show them to avoid overcrowding the figure. Therefore, both experiments show that the outcome fractions and their dependences on the gas density are consistent with the ranges and values physically allowed by the total energy (e.g., the 1+1+1+1 outcome only occurs for positive total energies).

We compare our results with the outcome probabilities at $n = 0\ \mathrm{cm}^{-3}$ and $E_0 = 0$ given in Leigh et al. (2016) (see Figure 4 at virial ratio $k \simeq 1$). These are marked as blue hollow dots using the same shape for each outcome. To avoid overlapping with other data points, these points are marked off the $E_0 = 0$ line (the vertical dotted line at $n = 10^2\ \mathrm{cm}^{-3}$). Note that the numerical scattering experiments in Leigh et al. (2016) agree with those shown here for $a_0 = 1$ AU since all assumptions are the same, including the semimajor axis ($a_0 = 1$ AU), the eccentricity ($e = 0$), the stellar mass ($M = 1\ \mathrm{M}_\odot$) and the total initial energy ($E = 0$). Additionally, we find that the outcome fractions in our study at $n = 10 - 10^2\ \mathrm{cm}^{-3}$ are still comparable to those found in Leigh et al. (2016), even for our other choices of the semimajor axis ($a_0 = 10$ AU and 100 AU). These results are consistent with our expectations in *region 1*. In this region, the gravitational forces between stars dominate, and hence the stellar dynamics should remain the same as in the absence of the background potential.

However, as the density increases, the final encounter outcomes and their probabilities change, due to the effect of the background potential, which acts to reset the zero-point of the total system energy.

The fractions, especially for $a_0 = 100$ AU, diverge slightly from the results for the other semimajor axes as n increases. We start to see that the ejected stars return toward the system CM in *region 2* (see Figure 2). Consequently, the stars take part in repeated scattering events that would not have occurred in the absence of a background potential. This leads to discrepancies in the final outcome probabilities relative to the no background potential case. This regime is different from the case where stellar interactions dominate, as it happens in *region 1*. Similarly, we find (see Figure 6) that the final velocity distributions for the ejected stars are shifted to lower velocities for $a_0 = 100$ AU. This could be because: 1) it is more likely that the simulations stall when the ejected stars slow down provided $r_\star < r_{\rm term} < r_{\rm return}$ in *region 2*; 2) in some cases the simulations reach a pre-set maximum computation time. In this case, slower velocities (a snapshot or instantaneous velocity sampled randomly over the entire oscillatory motion) happen to often be recorded as the final velocity. In order to understand if this only occurs for the $a_0 = 100$ AU case (largest initial value in the default range of densities) at the critical energy limit, we run another simulation with an even larger semimajor axis, $a_0 = 10^3$ AU, and negative total energy ($n = 10\ \mathrm{cm}^{-3}$). In this case, we might expect a similar behavior for the ejected stars in *region 2*. As before, we clearly see returning stars in this experiment. However, as marked by the green solid dots slightly off $n = 10\ \mathrm{cm}^{-3}$ (to avoid overlapping) in Figure 2, the cases with smaller semimajor axes have almost the same outcome probabilities. This is because the time taken for the ejected stars to come back and engage in another scattering event (i.e, the oscillation period indicated along the upper x-axis in Figure 2) is quite long. Hence, the number of encounters is insufficient to have a noticeable effect before the maximum simulation time is reached. Note that the total computation time includes the initial drop-in time at the onset of the simulations and the duration of the interaction before the final ejection event occurs. This can also help to explain why the outcome probabilities diverge more for higher n; that is, higher encounter frequency. From these experiments, we suggest that the depth of the potential is one of the essential factors in determining deviations from isolated stellar dynamics.

Interestingly, just above the zero-energy limit, the fraction of 2+1+1 outcomes decreases by about the same amount that the 1+1+1+1 outcome increases, whereas the fractions of the other two outcomes (3+1 and 2+2) remain the same. The probability of having a 1+1+1+1 outcome appears to be determined by whether or not all four stars are promptly ejected. In other words, if the stars are ejected one at a time, then a 1+1+1+1 outcome does not occur. This is because once a single star is ejected with positive kinetic energy, then the left-over system should have a negative total energy, which can never end up fully ionized (by energy conservation). Note, however, that if the initial total energy is positive and sufficiently large, it is possible that after an ejection event the remaining subsystem still has a positive total energy, and so can be reionized into single stars later on. If $n = 10^3\ \mathrm{cm}^{-3}$, then the total energy is much smaller than the typical kinetic energies of ejected single stars (estimated as $v_{\rm esc} \sim v_{\rm cri}$). Thus, we expect that the prompt ejection of all four stars is the only channel for full ionization. As the 1+1+1+1 outcome begins to appear, the fractions of all other outcomes decrease (by what appears to be a roughly constant fraction). Since the 2+1+1 outcome probability is the highest, its decrease looks especially significant.

One other point to note in the density range $n = 10\ \mathrm{cm}^{-3}$ to $n = 10^3\ \mathrm{cm}^{-3}$ is that the increase we find in the probability of having a 1+1+1+1 outcome (i.e., from 0 to 0.2) is relatively large compared to the results of other scattering experiments (i.e Mikkola 1983; Fregeau et al. 2004). This discrepancy is most likely due to the presence of the background potential, but the different choices for the impact parameter and eccentricity could also contribute. In our study, we only consider initially circular orbits and zero impact parameters (i.e., head-on collisions). However, other studies draw the eccentricity and impact parameter from specified distributions. For instance, when two binaries collide head-on there is a higher probability of full ionization occurring relative to encounters with non-zero impact parameter, since all four stars are more likely to interact strongly at the first encounter such that the two binaries would both be (at least temporarily) fully ionized. Therefore, initial configurations such as head-on collisions can increase the fraction of 1+1+1+1 outcomes. Meanwhile, the background potential serves to enhance the effects of gravitational focusing, drawing all stars toward the system CM.

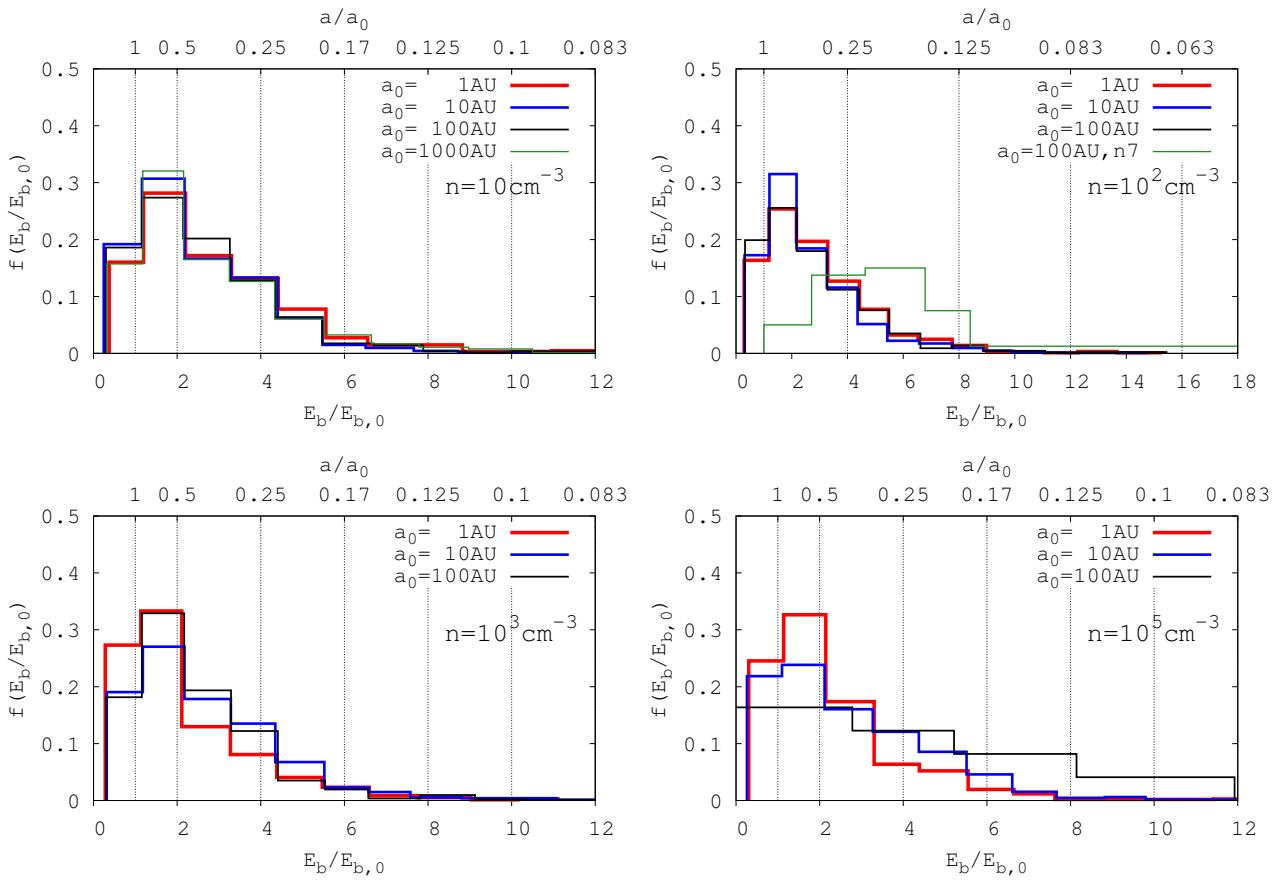

Figure 4. The binding energy distributions (scaled by the initial binary binding energy) for binaries formed during 2+1+1 outcomes, for number densities of $n = 10$ cm^{-3} to $n = 10^5$ cm^{-3} (from the *top left* to *bottom right* panels, forming a "Z" configuration). The red, blue and black solid lines correspond to, respectively, $a_0 = 1$ AU, 10 AU and 100 AU. Particularly, we also show the distribution for $n = 10^7$ cm^{-3} (green line) in the panel for $n = 10^2$ cm^{-3} since they have same total energy. The semimajor axis corresponding to a given binding energy is shown along the upper axis. We provide the best fits for $n = 10 - 10^3$ cm^{-3} in Table A1.

3.2.2 Exploring the strong-background potential, positive-energy regime

To explore the dynamical effects when the background potential is very strong, we further ran simulations with $n = 10^5$ cm^{-3} . As shown in Figure 2, each set of simulations at $n = 10^5$ cm^{-3} corresponds to a different region. From this we expect that the results from each set of simulations should reflect the characteristic behavior of the stars in the corresponding region. And this is exactly what we see from the outcome probabilities in Figure 3 and the binary binding energy distributions in the *bottom right* panel of Figure 4.

The outcome probabilities become different for each semimajor axis. This is different from the cases with $n = 10 - 10^3$ cm^{-3} in which each outcome probability for all the semimajor axes consistent within one or two standard deviations as long as n is same. More explicitly, for $a_0 = 1$ AU, these probabilities are almost the same as for $n = 10^3$ cm^{-3}. Since for this value of a_0 the gravitational forces between the stars still dominate over the background potential (*region 1*), the outcome probabilities are expected to remain the same as those for $n = 0$. Since the cross section for each outcome does not vary much (Sweatman 2007; van den Heuvel & Rappaport 1992) from $n = 10^3$ cm^{-3} to $n = 10^5$ cm^{-3} (0 - 0.04 in the unit of $E_{\rm b}(a = 1$ AU$)$), these outcome probabilities are reasonable. Notice that the units shown along the upper x-axis of the figure correspond to $E_{\rm b}(a = 100$ AU$)$. For $a_0 = 10$ AU, the outcome probabilities start to differ, similar to the cases for $n = 10^2$ and 10^3 cm^{-3} cases with $a_0 = 100$ AU (*region2*).

Interestingly, for $a_0 = 100$ AU, the outcome probabilities for 2+1+1 and 1+1+1+1 reverse and all other outcomes (3+1 and 2+2) are completely suppressed. For the cases with the 2+1+1 outcome, we find that subsequent stellar scatterings continue, but more frequently due to the stronger potential and hence higher accelerations, until two single stars are completely ejected from the system. Once a compact binary forms with sufficiently large binding energy, it survives successive encounters, becoming more and more compact via the slingshot mechanism. This also implies that it is more likely that a wide binary or triple will be ionized (i.e., the complete suppression of the 2+2 and 3+1 outcomes). In the presence of a deep potential, a single star has to gain a higher escape velocity for complete escape, necessarily leading to a hardened binary. Recall that $v_{\rm esc} \sim \sqrt{\rho}$ (see the additional termination criteria 6). As a result, we see a shift of the binding energy distribution towards the higher energy

range in the *bottom right* panel of Figure 4. Otherwise, like the cases with the 1+1+1+1 outcome, two binaries should be first ionized into four stars in order to escape.

We performed one additional experiment to more clearly understand the effects of the background potential on the subsequent stellar dynamics for negative total energies. In this experiment, we assume $a_0 = 100$ AU and $n = 10^7$ cm^{-3}. With these choices, we are able to find a system corresponding to *region 3* where the total energy is the same as for the case with $a_0 = 100$ AU, $n = 10^2$ cm^{-3} (i.e. $E_0 \simeq 0$), by adjusting $v_{\rm rel}$ and r_{12}. For this particular experiment, we set $M_{\rm gas} = 40$ M$_\odot$($r_{\rm bg} = 6600$ AU). This choice for the total gas mass is such that stars can escape from the background potential well and the effects of the background potential should be significant. In this experiment the only end product is 2+1+1 (cf. 2+1+1 and 1+1+1+1 in the simulation for $E_0 > 0$ with $n = 10^5$ cm^{-3} and $a_0 = 100$ AU). It is possible that two binaries are fully ionized but given the total energy budget available to all four single stars, they cannot have sufficiently high escape velocities (or kinetic energies) to meet the criterion for all four single stars to pass the outer potential boundary. We present the binding energy distribution for this case (green solid line) in the *top right* panel of Figure 4 ($n = 10^2$ cm^{-3}) since they share the same total energy E_0. The distribution is concentrated more toward higher binding energies, similar to the $n = 10^5$ cm^{-3} and $a_0 = 100$ AU case (black solid line in the *bottom right* panel). In addition, the final binaries are always more compact than the initial binaries (the maximum semimajor axis for the final binary is $a = 64$ AU $< a_0$ or, $E_b/E_{b,0} > 1$).

3.3 Statistical properties of the scattering products

In this section, we describe the statistical properties of the binaries and single stars formed in our simulations in the presence of a background potential for both the 2+1+1 and 2+2 outcomes. That is, we show the final distributions of binding energies (semimajor axes) and eccentricities for all binaries formed in our simulations, as well as the final relative velocities of the ejected single stars and the binary for the 2+1+1 outcome, and between the two binaries in the 2+2 outcome. We provide fitting formulae for all distributions, except for the velocity distributions, in Appendix A.

3.3.1 The 2+1+1 outcome

The 2+1+1 outcome has the highest probability of occurring, relative to the other outcomes. Unlike during full ionization (i.e., 1+1+1+1), the single star ejection events are not necessarily prompt. Typically, both binaries are temporarily ionized at first impact and one single star is ejected, leaving behind an unstable triple system, followed by the eventual ejection of the second single star. For the 2+1+1 outcome, the final total energy may be regarded as consisting of two components, namely the (negative) binding energy of the final binary and the (positive) kinetic energies of the two single stars and the binary (with respect to the system CM and ignoring the gravitational potential between the escaped objects). Since we are exploring the nearly zero energy limit, the final binding energy of the binary immediately tells us about the kinetic energies of the ejected single stars.

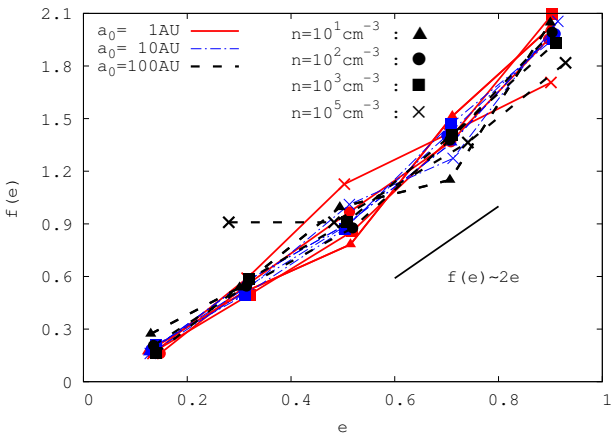

Figure 5. The eccentricity distributions for binaries formed during 2+1+1 outcomes, for all number densities and semimajor axes. The same colors are used as in Figure 4. All distributions follow a thermal distribution function, $f(e) \sim 2e$, except for $n = 10^5$ with $a_0 = 100$ AU, the set corresponding to *region 3*).

Figures 4 and 5 show the distributions of final binary binding energies and eccentricities for each gas density and initial semimajor axis. In all four panels of Figure 4, the red, blue and black solid lines correspond to, respectively, the initial semimajor axes $a_0 = 1$ AU, 10 AU and 100 AU. The distribution for $a_0 = 100$ AU and $n = 10^7$ cm^{-3} is depicted by the green solid line in the *top right* panel. The same colors are used for the initial semimajor axes as in Figure 5.

The final binary properties share several things in common independent of the gas density and initial semimajor axis. First, the final binary binding energy distribution has a peak at $E \simeq E_{\rm b,0}$, which corresponds to a semimajor axis for the final binary that is identical to the initial semimajor axis. That is, the binding energies of the two (identical) initial binaries determine that of the final binary. We find consistent results for the final relative velocities for the ejected single stars with respect to the final binary, in the sense that energy and momentum are conserved. The *left* column in Figure 6 presents the final relative velocity distributions of single stars in the 2+1+1 case. The same line colors and types are used in both columns as in Figure 4. The distributions have their peak at $v \simeq 0.6\ v_{\rm cri}$. Recall that, when $E_0 \sim 0$, the absolute value of the binding energy is equal to the sum of the total kinetic energies of the ejected single stars in the frame of reference of the final binary (with reduced mass 2/3 M$_\odot$). We can also compare the final binary binding energy distribution for $E_0 = 0$ ($n = 10^2$ cm^{-3} in the *upper right* panel) with the ejection velocity distribution without a background potential in Leigh et al. (2016) ($k = 1$ in their Figure 10), for the 2+1+1 outcome. Given that they find the same ejection velocities for both single stars in their ejection velocity distributions, corresponding to $KE(v_{\rm rel} = 1) = |E_b|$ and $v_{\rm cri}(a_0 = 1$ AU$) = 42$ km s^{-1}, we find good agreement with Leigh et al. (2016). Second, all final binding energy distributions extend up to $\sim 12E/E_{b,0}$. This implies that the semimajor axis corresponding to the most compact binary

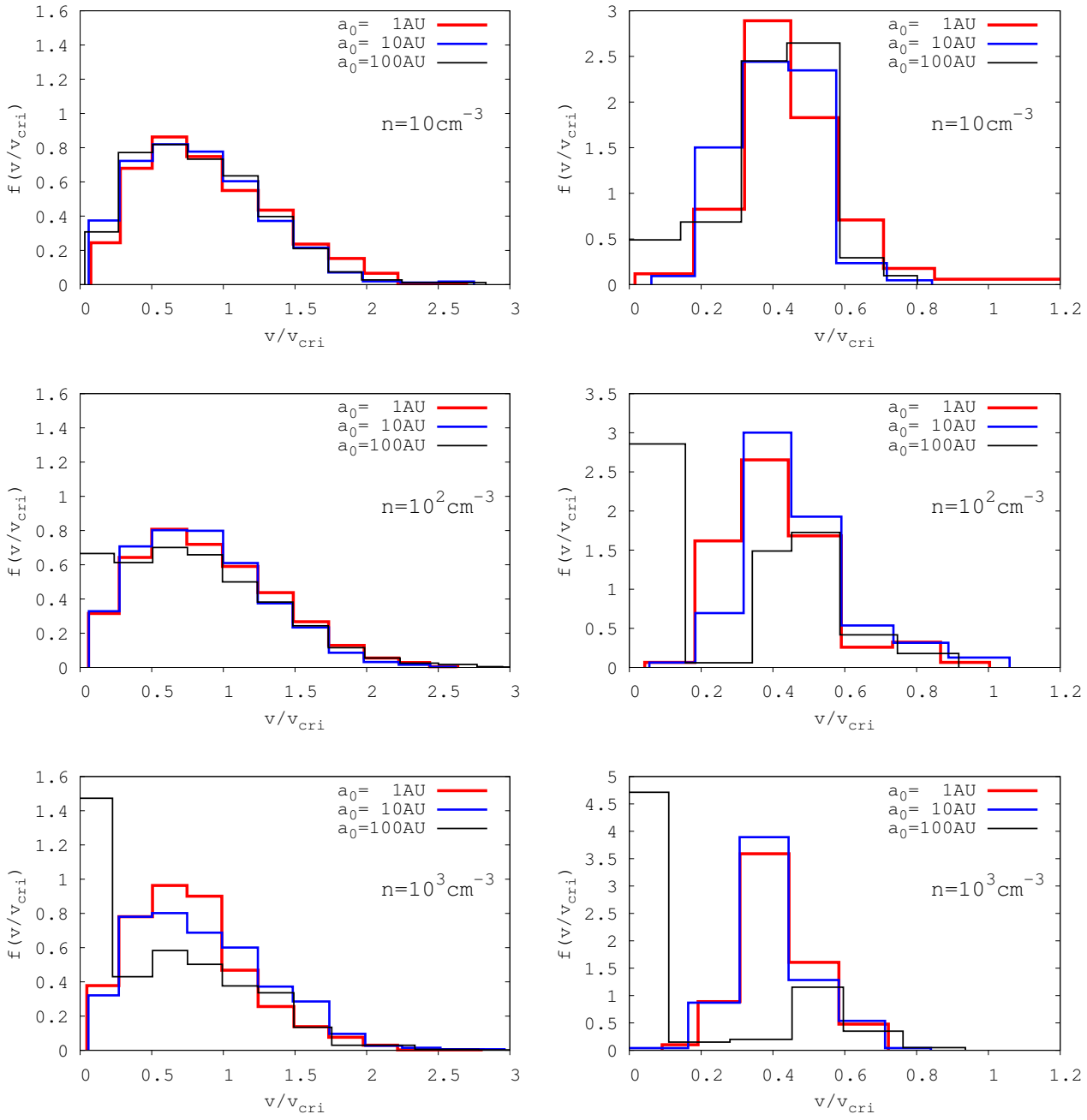

Figure 6. The final velocity distributions (scaled with $v_{\rm cri}$) for binaries formed during 2+1+1 outcomes (*left* column) and 2+2 outcomes (*right* column), for number densities of $n = 10$ cm^{-3} to $n = 10^3$ cm^{-3} (from *top* to *bottom* panel). In both panels, the same colors are used as in Figure 4.

that can possibly form via a head-on collision at such high relative velocity is $\sim 1/12$ the initial semimajor axis. Third, given the low probability for $E < E_{b,0}$, the final binaries tend to be more compact than the initial binaries. But note that collisions with two binaries of unequal size and non-zero impact parameter may yield different results. Finally, the eccentricity distributions in Figure 5 approximately follow a thermally-averaged density function (Heggie 1975), or:

$$f(e) \sim 2e. \quad (19)$$

Interestingly, this is what is typically found for the binary eccentricity distributions formed during three-body scatterings experiments (i.e Mikkola 1994; Valtonen & Karttunen 2006). At least for the 2+1+1 outcome, four-body scatterings produce the same eccentricity distribution. With that said, we emphasize caution in concluding from this that a thermal distribution applies to all four-body scatterings. In particular, we will show a somewhat different eccentricity distribution for binaries formed during 2+2 outcomes in the following section. It is possible that the repeated scatterings (*region 3*) are responsible for a slight departure for the $n = 10^5$ case with $a_0 = 100$ AU (black dashed line with

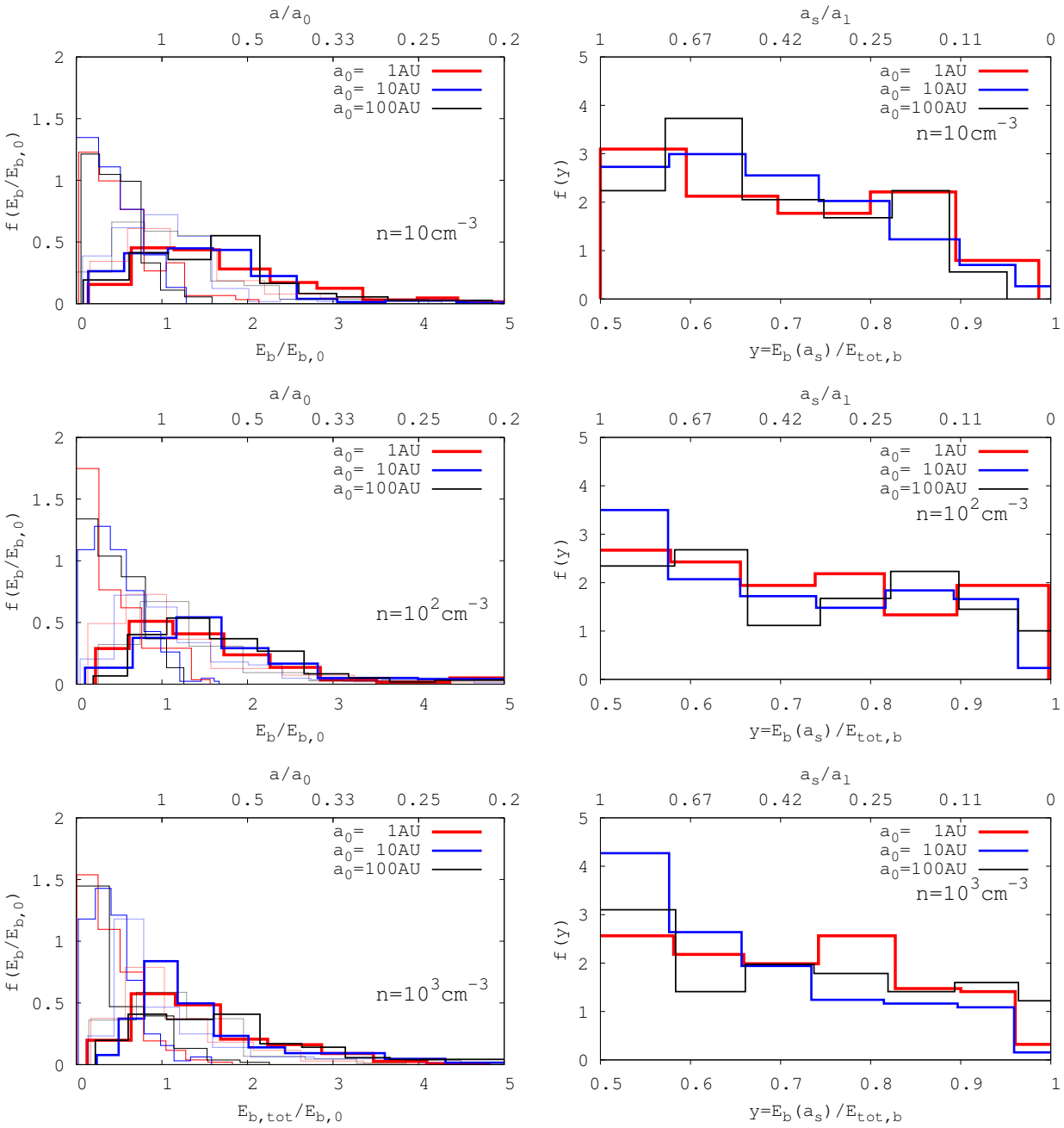

Figure 8. The final total binary binding energy distributions ($E_{\rm b,tot}$) are shown with thick solid lines in the *left* panel, and the fraction of this total $E_{\rm b,tot}$ assigned to the more compact binary is shown in the *right panel* for number densities of $n = 10$ cm^{-3} to $n = 10^3$ cm^{-3} (from the *top* to *bottom* panels). In the *left* panel, for comparison we over plot the distributions for each individual binary shown in Figure 7 with thinner lines. The semimajor axis estimated from each final binding energy is indicated along the upper x-axis. In both panels, the same colors are used as in Figure 4. We provide the best fits for both distributions in Table A3 and A4.

cross mark) relative to the other cases. But, we cannot rule out statistical errors as being the primary effect here.

We find the best fits for the binding energy distributions assuming two different functional forms in Appendix A. Motivated by Mikkola (1983), but with more free parameters (a, b, c and d), we use the following expression:

$$f(x) \sim x(a + bx^c)^d. \quad (20)$$

For an alternative functional form, we use the skew normal distribution function, defined as the product of a normal distribution $\phi(x, \bar{x}, \sigma_x)$ and an accumulative normal distribution $\Phi(\xi, x, \bar{x}, \sigma_x)$ for a random variable x with skewness ξ, or:

$$f(x) \sim \phi(x, \bar{x}, \sigma_x)\Phi(\xi, x, \bar{x}, \sigma_x)\,. \quad (21)$$

All free parameters (a to d and $\bar{x}$, σ_x and ξ) and the full expressions for the normal distribution $\phi(x, \bar{x}, \sigma_x)$ and accumulative normal distribution $\Phi(\xi, x, \bar{x}, \sigma_x)$ are summarized in Tables A1 and A2.

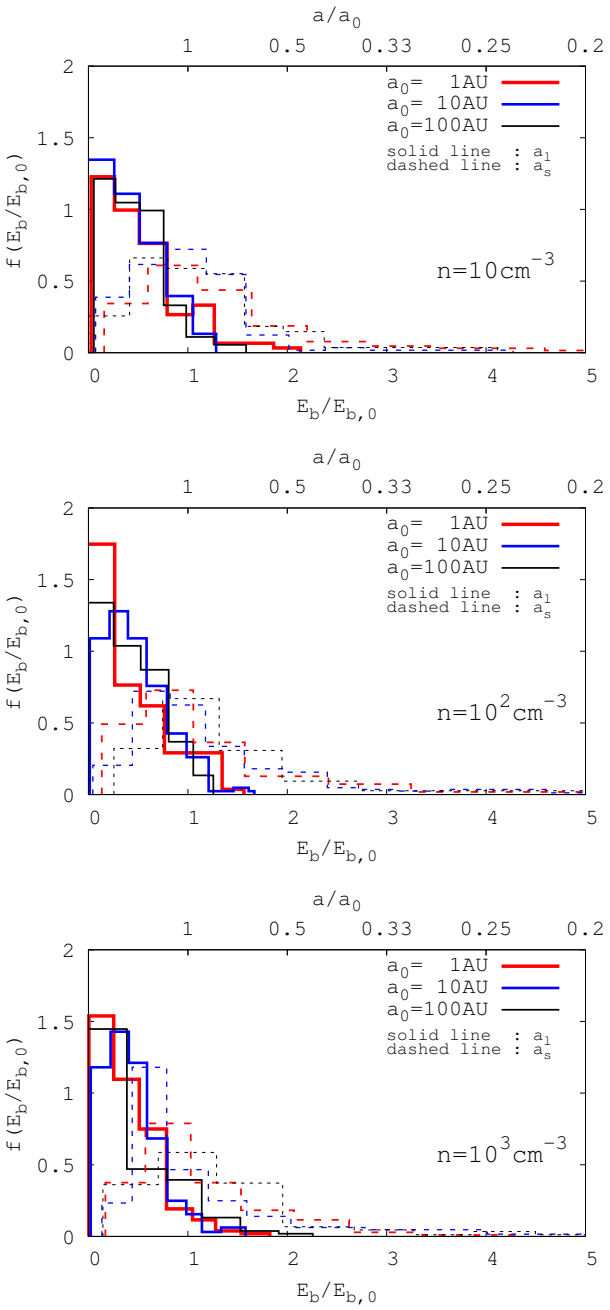

Figure 7. The final binary binding energy distributions for both binaries produced during 2+2 outcomes for number densities of $n = 10$ cm^{-3} to $n = 10^3$ cm^{-3} (from the *top* to *bottom* panels). We adopt the same colors as used in Figure 4, but different line types are used to distinguish between the smaller or more compact binary ($a_{\rm s}$, dashed line) and the larger or less compact binary ($a_{\rm l}$, solid line). The semimajor axis estimated from the binding energy is shown along the upper x-axis. We provide the best fits in Table A3.

3.3.2 The 2+2 outcome

The 2+2 outcome has the second highest probability of occurring, at least until the 1+1+1+1 outcome dramatically escalates at $n = 10^3$ cm^{-3}. Here, binary formation is suppressed due to the dissociation of any wide binary by single stars when the stars are all trapped deep within the background potential. In the CM frame of the two final binaries, both binaries are ejected in opposite directions with the same velocity. Only the final binary binding energies and/or eccentricities change. Since no single stars are formed during the 2+2 outcome, the total encounter energy can be decomposed into four components. That is, letting $a_{\rm l}$ and $a_{\rm s}$ represent the semimajor axis of the larger and smaller binary, respectively, the total energy is:

$$E = E_{\rm b,tot} + KE_{\rm tot} \quad (22)$$
$$= E_{\rm b}(a_{\rm s}) + E_{\rm b}(a_{\rm l}) + KE(a_{\rm s}) + KE(a_{\rm l}) \quad (23)$$

where $E_{\rm b,tot}$ is the total binding energy (equal to the sum of the binding energies of the two binaries, or $E_{\rm b}(a_{\rm s}) + E_{\rm b}(a_{\rm l})$) and $KE_{\rm tot}$ is the total kinetic energy (equal to the sum of the kinetic energies of the two binaries, or $KE(a_{\rm s}) + KE(a_{\rm l})$).

In Figure 7, we compare the binding energies of the two binaries formed during the 2+2 outcome, as a function of the gas density and the initial semimajor axis. The same color scheme is adopted as in Figure 4, but two different line types are used to distinguish between the more (dashed line) and less (solid line) compact binary. The distribution for $a_{\rm l}$ tends to be concentrated in the range $E_b/E_{b,0} < 1$, which implies that the wider binary is less compact than the initial binary. The distribution for $a_{\rm s}$, on the other hand, peaks at $E_b/E_{b,0} \simeq 1$. Note that the overall shapes of the semimajor axis distributions are different than what we found for binaries formed during 2+1+1 outcomes (see Figure 4).

Importantly, as shown in Figure 7, studying the binding energy distributions of each binary does not allow us to study the relationship between the two final binaries resulting from a particular interaction. To correct this, in Figure 8 we present the total binding energy ($E_{\rm b,tot}$) distribution of the two binaries combined (the thick solid line in the *left* panel) and the fraction of the total binding energy assigned to the most compact binary (y defined in equation 24 below) The *right panels* show the results for number densities $n = 10$ cm^{-3} to $n = 10^3$ cm^{-3} (from *top* to *bottom*). For comparison, we over plot in the *left* panel the distributions for each individual binary (first shown in Figure 7) with thinner lines. The semimajor axis associated with a given binding energy is indicated along the upper x-axis.

As seen in the *left* panels, in which we combine the binding energy budgets from both binaries, $E_{\rm b,tot}$ reaches its maximum probability at $E_b/E_{b,0} \simeq 1 - 2$. This is typically the binding energy associated with each binary when they are ejected from each other at a relative velocity comparable to the escape velocity ($v_{\rm esc}$, which in our case is $v_{\rm esc} \geqslant v_{\rm cri}$). Interestingly, the high-energy tail in the 2+1+1 outcome distribution extends farther (i.e., out to $E_b/E_{b,0} \simeq 11 - 12$) than in the 2+2 outcome distribution, which drops off rapidly at $E_b/E_{b,0} \simeq 5 - 6$. This is because the two single stars produced during the 2+1+1 outcome leave with more positive energy (in the form of kinetic energy), leaving a larger reservoir of negative energy for the final binary binding energy, relative to the 2+2 case. Using a skew normal distribution, we obtain the best fitting parameters for the binding energy distribution of each binary, as well as the total binding energy distribution. These fit parameters are summarized in Table A3.

When the encounter is over, each binary takes some fraction of the total binary binding energy. This is shown in the *right* panels. Here, we introduce a variable y, defined as

the fraction of the total binding energy assigned to the more compact binary:

$$y = \frac{E_{\rm b}(a_{\rm s})}{E_{\rm tot,b}} \tag{24}$$

$$= \frac{a_{\rm l}}{a_{\rm s}+a_{\rm l}} = \frac{1}{a_{\rm s}/a_{\rm l}+1} \tag{25}$$

The ratio $a_{\rm s}/a_{\rm l}$ corresponding to a given value of y is marked along the upper x-axis. As y approaches 0.5 (i.e., $a_{\rm s}/a_{\rm l} \simeq 1$), the two binaries share similar fractions of the total binary binding energy (50% for each binary), and their semimajor axes are comparable. However, if y approaches unity, then one binary has most of the total binary binding energy; we are left with one compact binary and one wide binary. We find that the distributions decrease as y increases, implying that there are fewer outcomes in which one of the binaries ends up with most of the total binding energy. In Table A4, the best fitting values to these distributions are reported, using the relation:

$$f(y) = \alpha y + \beta \tag{26}$$

Note that the slope α is always negative.

Finally, we show the eccentricity distributions for both binaries formed during 2+2 outcomes in Figure 9. The same color scheme is used as before, but the solid and dashed lines correspond to the less ($a = a_{\rm l}$) and more ($a = a_{\rm s}$) compact binary, respectively. The eccentricity distribution of the less compact binary does not follow the thermally averaged form (Equation 19). To characterize these distributions, we fit to the simulations the following general functional form with a free parameter λ:

$$f(e) \sim e^{\lambda} \tag{27}$$

The average value of λ for $e(a_{\rm l})$ exceeds 2.3, whereas that for $e(a_{\rm s})$ is around $1.3-2.0$. Both of these values are larger than 1, which implies more eccentric binaries relative to the thermally averaged density function. We speculate that a value for b larger than 1 arises due to conservation of angular momentum and energy, and the fact that a larger value for the semimajor axis requires a higher eccentricity to conserve angular momentum. The resulting values for λ are given in Table A5.

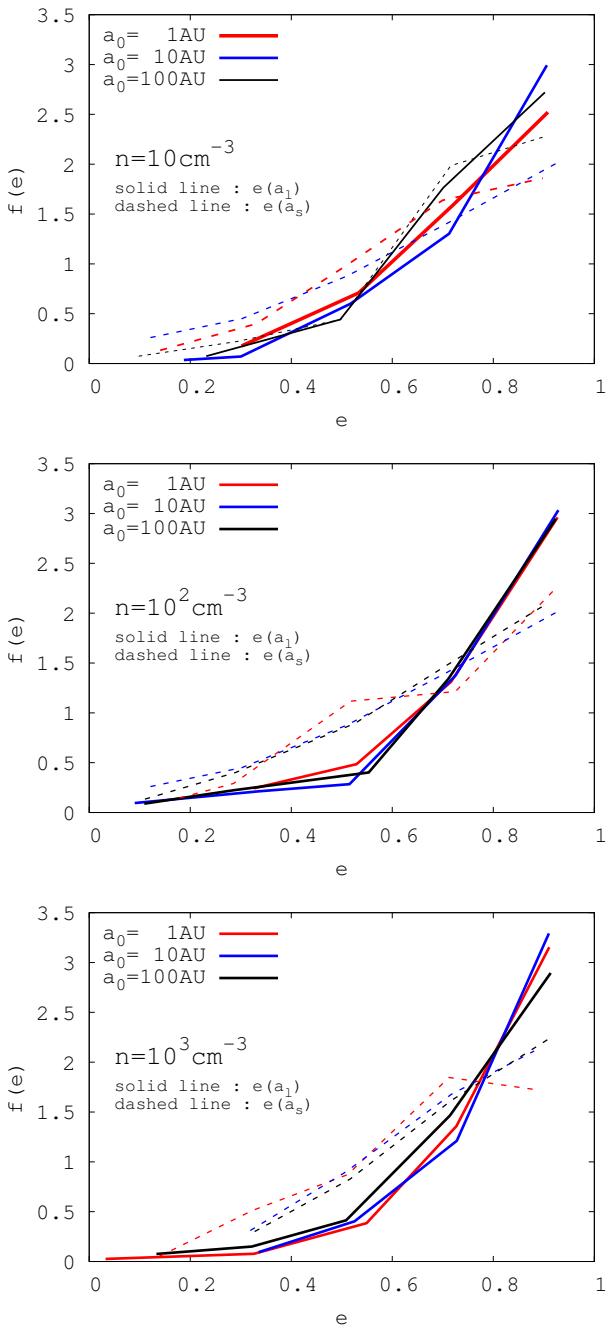

Figure 9. The eccentricity distributions are shown for binaries formed during 2+2 outcomes, for number densities ranging from $n = 10$ cm^{-3} to $n = 10^3$ cm^{-3} (from *top* to *bottom*) and different semimajor axes. The solid and dashed lines correspond to the less and more compact binary, respectively. The same color scheme is used as in Figure 4. Note that all eccentricity distributions follow the thermally averaged density function. The best-fitting values of the parameter λ are given in Table A4.

4 DISCUSSION AND SUMMARY

We have performed binary-binary scattering experiments in the presence of a background gravitational potential. The background is taken to be an uniform gas medium, for simplicity. However, we emphasize that only the gravitational effects of the background potential are considered. The potential remains static in time, and no gas damping (e.g., dynamical friction, accretion) can occur. We explore a range of potential strengths corresponding to gas densities of $n = 10$ cm^{-3} to 10^5 cm^{-3} for three distinct values of the semimajor axis, namely $a = 1$ AU, 10 AU and 100 AU. Additional simulations with other values of a_0 and n were performed when needed.

We find that the effect of the background potential on the scattering products depends on both the total energy of the system (whose zero-point is reset by the potential), as well as on its relative strength compared to the potential generated by the single stars.

We summarize the effects of the background potential as follows:

(i) For any non-zero gas density n, the role of the background potential is to *reset the zero-point of the total system*

energy. Accordingly, this affects the types and properties of the objects (single, binary and/or triple stars) formed during the interactions as well as their outcome probabilities. Since the contribution from the background potential to the total system energy is always positive (for our assumption of an uniform medium), it acts to decrease the zero-point of the total system energy.

(ii) In order to isolate the various effects, and in particular the relative role played by the initial binary semimajor axis a_0 for a given gas density n, we have introduced three characteristic radii ($r_\star$, $r_{\rm return}$ and $r_{\rm bg}$), defined relative to the system CM. These radii define three distinct regions (*region 1*, *region 2* and *region 3*, from the innermost to the outermost one), and play an important role relative to R, the typical inter-particle separation during the scattering simulations in dense stellar environments.

If $R < r_\star$, the stellar interactions are confined to a region where the stellar gravitational potential dominates over the contribution from the background gas potential. Hence, in this case, the effect of the background potential on the coincident stellar dynamics is negligible. The sets of experiments with (n, a_0)=($10 - 10^2$ cm^{-3}, $1 - 100$ AU) and (10^3 cm^{-3}, $1 - 10$ AU) correspond to this regime. The outcome probabilities, as well as the types and properties of the products, *look reasonably similar to the analogous experiments without a background potential*. We compared our results with Leigh et al. (2016). They performed binary-binary scattering experiments exploring a range of values for the initial virial ratio. Our simulations with $n = 10 - 10^2$ cm^{-3} and $a_0 = 1$ AU show good agreement with their results.

If $r_\star < R \leqslant r_{\rm return}$, stars in this region begin to slow down as they feel the gravitational influence of the background potential (i.e., the enclosed gas mass starts to become comparable to the stellar mass). We see this in the final velocity distributions in Figure 6. For $n = 10^3$ cm^{-3} and $a_0 = 100$ AU, the final velocity distributions are shifted to lower velocities. Even in this region, it is possible that stars become bound to the gas and return toward the system CM to go through additional scattering events. These scatterings act to ionize wide binaries and triples. Accordingly, this results in discrepancies in the outcome probabilities relative to the lower semimajor axis runs. Note, however, that our simulations do not show noticeable differences in the final binary properties. As we explain in detail in the next paragraph, the large differences appear with the emergence of very compact binaries due to numerous subsequent encounters. Hence, perhaps the number of encounters is insufficient for this to occur. That is, since the ionization of the wide binaries or triples precedes the formation of the compact binaries, the outcome probabilities may start to change before the distributions do.

If $r_{\rm return} \leqslant R$, the background potential acts to "filter out" certain outcomes at a given total energy. This is usually the case for high values of the gas density n. Due to the deep background potential well, stars remain bound to the gas and continue to interact until eventually they are ejected at sufficiently high velocity to become unbound and escape to infinity. This requires strong, close gravitational interactions for the stars to gain these high ejection velocities. Triples and wide binaries tend to form with low recoil velocities, such that they almost always remain bound to the background potential and return to undergo subsequent scattering events. This process continues until eventually two single stars are ejected at high velocity, leaving behind a compact binary. *Thus, in a deep background potential, stable triples and wide binaries are unlikely to form during binary-binary interactions. Instead, the interactions tend to produce a very compact binary and two high-velocity single stars.* As a result, we see a shift in the binding energy distributions toward a higher energy range, and outcome probabilities around zero for the 2+2 and 3+1 outcomes. This is for the two sets of simulations with (n, a_0)=(10^5 cm^{-3}, 100 AU) and (10^7 cm^{-3}, 100 AU).

(iii) The presence of the background potential can act to prolong the encounter durations. This is important in real astrophysical environments, and if one considers finite-sized particles. For example, the presence of the gas medium adds mass and increases the gravitationally-focused cross-section for encounters with other stars in a star cluster. This leads to a non-negligible probability that the interactions will be interrupted (Geller & Leigh 2015). This is especially true in astrophysical systems with moderate stellar densities, such as the cores of open clusters. Here, binary-binary encounters should be frequently interrupted by other stars and binaries in the cluster (Geller & Leigh 2015). If the encounters last longer, then the probability of a direct physical collision occurring also increases (Leigh & Geller 2012, 2015). This naively predicts that collisions and/or mergers should happen more frequently during stellar dynamical interactions occurring in dense gaseous environments.

(iv) In summary, we have discussed the stellar dynamics in a continuous background potential assuming an uniform gas medium. We have shown from the changes in the outcome probabilities that the presence of the background potential resets the zero-point of the total system energy. Furthermore, based on the three characteristic distances ($r_{\rm star}$, $r_{\rm return}$ and $r_{\rm gas}$) which quantify the volume corresponding to each of the three regions, we find a relation between a_0 and n (equation 18). This relation, in turn, allows us to identify when the background potential makes significant impacts on the dynamics between stars, that is, when the presence of the gas causes deviations from what should be expected for the 4-body dynamics in isolation.

Acknowledgements We are grateful to the referee for constructive and meaningful comments. Results in this paper were obtained using the high-performance LIred computing system at the Institute for Advanced Computational Science at Stony Brook University, which was obtained through the Empire State Development grant NYS #28451.

REFERENCES

Abbott B. P. et al., 2016, ApJL, 818, L22
Abt H. A., Levy S. G., 1976, ApJ Supp., 30, 273
Albrow M. D., Gilliland R. L., Brown T. M., Edmonds P. D., Guhathakurta P., Sarajedini A., 2001, ApJ, 559, 1060
Antognini J. M. O., Thompson T. A., 2016, M.N.R.A.S., 456, 4219
Bailyn C. D., 1989, ApJ, 341, 175

Belczynski K., Ryu T., Perna R., Berti E., Tanaka T. L., Bulik T., 2016, ArXiv e-prints
Brown R. L., Zuckerman B., 1975, ApJL, 202, L125
Cool A. M., Bolton A. S., 2002, in Astronomical Society of the Pacific Conference Series, Vol. 263, Stellar Collisions, Mergers and their Consequences, Shara M. M., ed., p. 163
Davies M. B., Piotto G., de Angeli F., 2004, M.N.R.A.S., 349, 129
Duquennoy A., Mayor M., 1991, A&A, 248, 485
Erwin F., 1969, NASA Technical Report, 315, 1
Fregeau J. M., Cheung P., Portegies Zwart S. F., Rasio F. A., 2004, M.N.R.A.S., 352, 1
Geller A. M., Leigh N. W. C., 2015, ApJL, 808, L25
Gratton R. G., Carretta E., Bragaglia A., 2012, A&A Rev., 20, 50
Halbwachs J. L., Mayor M., Udry S., Arenou F., 2003, A&A, 397, 159
Heggie D., Hut P., 2003, The Gravitational Million-Body Problem: A Multidisciplinary Approach to Star Cluster Dynamics
Heggie D. C., 1975, M.N.R.A.S., 173, 729
Heggie D. C., Hut P., 1993, ApJ Supp., 85, 347
Heggie D. C., Hut P., McMillan S. L. W., 1996, ApJ, 467, 359
Hills J. G., Day C. A., 1976, ApL, 17, 87
Hut P., 1985, in IAU Symposium, Vol. 113, Dynamics of Star Clusters, Goodman J., Hut P., eds., pp. 231–247
Hut P., Verbunt F., 1983, Nat., 301, 587
Ji J., Bregman J. N., 2015, ApJ, 807, 32
Knigge C., Leigh N., Sills A., 2009, Nat., 457, 288
Leigh N., Geller A. M., 2012, M.N.R.A.S., 425, 2369
Leigh N., Sills A., 2011, M.N.R.A.S., 410, 2370
Leigh N., Sills A., Knigge C., 2007, ApJ, 661, 210
Leigh N. W. C., Geller A. M., 2013, M.N.R.A.S., 432, 2474
—, 2015, M.N.R.A.S., 450, 1724
Leigh N. W. C., Giersz M., Marks M., Webb J. J., Hypki A., Heinke C. O., Kroupa P., Sills A., 2015, M.N.R.A.S., 446, 226
Leigh N. W. C., Stone N. C., Geller A. M., Shara M. M., Muddu H., Solano-Oropeza D., Thomas Y., 2016, M.N.R.A.S., 463, 3311
Leonard P. J. T., 1989, AJ, 98, 217
Lin D. N. C., Murray S. D., 2007, ApJ, 661, 779
Mikkola S., 1983, M.N.R.A.S., 203, 1107
—, 1984, M.N.R.A.S., 207, 115
—, 1994, M.N.R.A.S., 269, 127
Portegies Zwart S. F., McMillan S. L. W., 2000, ApJL, 528, L17
Reid I. N., Gizis J. E., 1997, AJ, 113, 2246
Rubenstein E. P., Bailyn C. D., 1997, ApJ, 474, 701
Ryu T., Tanaka T. L., Perna R., 2016, M.N.R.A.S., 456, 223
Samson W. B., 1975, A&Sp.Sc., 34, 363
Sana H., Gosset E., Evans C. J., 2009, M.N.R.A.S., 400, 1479
Sana H., Gosset E., Nazé Y., Rauw G., Linder N., 2008, M.N.R.A.S., 386, 447
Sana H., James G., Gosset E., 2011, M.N.R.A.S., 416, 817
Sigurdsson S., Phinney E. S., 1993, ApJ, 415, 631
Sollima A., Carballo-Bello J. A., Beccari G., Ferraro F. R., Pecci F. F., Lanzoni B., 2010, M.N.R.A.S., 401, 577
Subramaniam A., Gorti U., Sagar R., Bhatt H. C., 1995, A&A, 302, 86
Sweatman W. L., 2007, M.N.R.A.S., 377, 459
The LIGO Scientific Collaboration et al., 2016, ArXiv e-prints
Valtonen M., Karttunen H., 2006, The Three-Body Problem
van den Heuvel E. P. J., Rappaport S. A., eds., 1992, NATO Advanced Science Institutes (ASI) Series C, Vol. 377, X-Ray binaries and recycled pulsars

APPENDIX A: FITTING FORMULAE FOR DISTRIBUTION FUNCTIONS

We provide the best fits for the binding energy and eccentricity distributions shown in the text for the 2+1+1 and 2+2 outcomes.

A1 2+1+1 case

For the binding energy, we fit two functional forms. First, motivated by Mikkola (1983) but with more free parameters (a, b, c and d), we use the following:

$$f(x) \sim x(a + bx^c)^d. \tag{A1}$$

For the second fit, we use the skew normal distribution function, defined as the product of a normal distribution $\phi(x, \bar{x}, \sigma_x)$ and an accumulative normal distribution $\Phi(\xi, x, \bar{x}, \sigma_x)$ for a random variable x with skewness ξ,

$$f(x) \sim \phi(x, \bar{x}, \sigma_x)\Phi(\xi, x, \bar{x}, \sigma_x) \tag{A2}$$

All free parameters (a to d and $\bar{x}$, σ_x and ξ) and the full expressions for the normal distribution $\phi(x, \bar{x}, \sigma_x)$ and accumulative normal distribution $\Phi(\xi, x, \bar{x}, \sigma_x)$ are summarized in Table A1 and A2. We take the skewness $\xi = 1$. The eccentricities for the 2+1+1 outcome follow a thermally averaged density distribution, $f(e) \sim e$ (equation 19).

	$n = 10$ cm^{-3}			$n = 10^2$ cm^{-3}			$n = 10^2$ cm^{-3}		
a_0	1 AU	10 AU	100 AU	1 AU	10 AU	100 AU	1 AU	10 AU	100 AU
a	1.0743	0.8307	0.9667	0.9351	0.9344	0.6465	0.0659	0.1035	1.6222×10^{-4}
b	0.0235	0.0851	0.0399	0.0635	0.0353	0.0583	0.01212	8.0138×10^{-3}	6.0042×10^{-6}
c	1.4334	2.6455	1.6667	1.8940	4.1905	1.5036	4.8179	1.7381	4.1526
d	-15.1900	-1.5990	-6.9951	-3.2957	-0.9147	-4.7687	-0.6612	-3.9653	-0.9783

Table A1. Best fits for the binding energy distributions for the 2+1+1 outcome with $f(x) \sim x(a + bx^c)^d$.

$x = E_{\rm b}/E_{\rm b,0}$	$n = 10$ cm^{-3}			$n = 10^2$ cm^{-3}			$n = 10^2$ cm^{-3}		
a_0	1 AU	10 AU	100 AU	1 AU	10 AU	100 AU	1 AU	10 AU	100 AU
$\bar{x}$	2.5749	2.2940	2.4367	2.6379	2.3373	2.2748	1.7118	2.3937	2.3000
σ_x	2.0790	1.7851	1.7848	1.9925	1.4324	2.2126	1.3159	1.9919	1.3764

Table A2. Best fits for the binding energy distributions for the 2+1+1 outcome with the skew normal distribution $f(x) \sim \phi(x, \bar{x}, \sigma_x)\Phi(\xi, x, \bar{x}, \sigma_x)$ where $\phi(x, \bar{x}, \sigma_x) = \frac{1}{\sqrt{2\pi\sigma_x^2}} e^{-(x-\bar{x})^2/\sigma_x^2}$ and $\Phi(\xi, x, \bar{x}, \sigma_x) = \int_\infty^{\xi(x-\bar{x})/\sigma_x} e^{-\frac{t^2}{2}}\, dt = \frac{1}{2}\Big[1 + {\rm erf}\Big(\xi \frac{x-\bar{x}}{\sqrt{2}\sigma_x}\Big)\Big]$. We take the skewness $\alpha = 1.0$.

A2 2+2 case

For the binding energies of each binary (wide and compact) and the total binding energy ($E_{\rm t,tot}$), we use the skew normal distribution function. This is the same as used for the binding energy distribution for the 2+1+1 outcome. The average values and the standard deviations of our best fits are summarized in Table A3. We also take the skewness $\xi = 1$.

Next, we define the variable y as the fraction of the binding energy assigned to the more compact binary. Each binary takes some fraction of the total binding energy,

$$y = \frac{E_{\rm b}(a_{\rm s})}{E_{\rm tot,b}} \tag{A3}$$

$$= \frac{a_{\rm l}}{a_{\rm s} + a_{\rm l}} = \frac{1}{a_{\rm s}/a_{\rm l} + 1}\,. \tag{A4}$$

For the best fit, we use the following formula,

$$f(y) = \alpha y + \beta\,. \tag{A5}$$

Two parameters α (slope) and β (intercept) in Table A4.

Finally, for the eccentricities of each binary (wide and compact), we fit to the simulations the following general functional form with a free parameter λ:

$$f(e) \sim e^{\lambda} \tag{A6}$$

the values for λ are given in Table A5. Maximum and minimum values for e are written below each value of λ.

$x = E_{\rm b}/E_{\rm b,0}$		$a_0 = 1$ AU			$a_0 = 10$ AU			$a_0 = 100$ AU		
		$a_{\rm s}$	$a_{\rm l}$	total	$a_{\rm s}$	$a_{\rm l}$	total	$a_{\rm s}$	$a_{\rm l}$	total
$n = 10$ cm^{-3}	$\bar{x}$	1.169$\pm$0.037	0.204$\pm$0.192	1.634$\pm$0.087	1.065$\pm$0.028	0.277$\pm$0.048	1.540$\pm$0.051	1.130$\pm$0.060	0.427$\pm$0.082	1.738$\pm$0.116
	σ_x	0.640$\pm$0.048	0.642$\pm$0.133	0.892$\pm$0.103	0.570$\pm$0.033	0.539$\pm$0.0451	0.862$\pm$0.064	0.628$\pm$0.071	0.425$\pm$0.107	0.832$\pm$0.138
$n = 10^2$ cm^{-3}	$\bar{x}$	0.937$\pm$0.030	-5.022$\pm$30.82	1.368$\pm$0.052	0.994$\pm$0.045	0.441$\pm$0.013	1.632$\pm$0.041	1.229$\pm$0.030	0.297$\pm$0.136	1.699$\pm$0.086
	σ_x	0.527$\pm$0.039	1.561$\pm$4.294	0.831$\pm$0.076	0.472$\pm$0.049	0.428$\pm$0.017	0.693$\pm$0.044	0.517$\pm$0.032	0.558$\pm$0.133	0.773$\pm$0.089
$n = 10^3$ cm^{-3}	$\bar{x}$	0.984$\pm$0.056	0.177$\pm$0.106	1.355$\pm$0.082	0.750$\pm$0.029	0.420$\pm$0.009	1.210$\pm$0.044	1.228$\pm$0.028	-4.791$\pm$23.9	1.698$\pm$0.084
	σ_x	0.450$\pm$0.063	0.504$\pm$0.077	0.641$\pm$0.092	0.233$\pm$0.028	0.334$\pm$0.012	0.402$\pm$0.045	0.657$\pm$0.034	1.610$\pm$3.523	0.992$\pm$0.111

Table A3. Best fits for the binding energy distributions for the 2+2 outcome with the skew normal distribution $f(x) \sim \phi(x,\bar{x},\sigma_x)\Phi(\xi,x,\bar{x},\sigma_x)$ where $\phi(x,\bar{x},\sigma_x) = \frac{1}{\sqrt{2\pi\sigma_x^2}} e^{-(x-\bar{x})^2/\sigma_x^2}$ and $\Phi(\xi,x,\bar{x},\sigma_x) = \int_{\infty}^{\xi(x-\bar{x})/\sigma_x} e^{-\frac{t^2}{2}} dt = \frac{1}{2}\Big[1 + {\rm erf}\Big(\xi\frac{x-\bar{x}}{\sqrt{2}\sigma_x}\Big)\Big]$. We take the skewness $\alpha = 1.0$.

y	$n = 10$ cm^{-3}			$n = 10^2$ cm^{-3}			$n = 10^2$ cm^{-3}		
a_0	1 AU	10 AU	100 AU	1 AU	10 AU	100 AU	1 AU	10 AU	100 AU
slope α	-4.516$\pm$1.606	-6.132$\pm$0.834	-4.775$\pm$2.519	-2.253$\pm$1.039	-4.804$\pm$1.406	-2.477$\pm$1.353	-3.963$\pm$1.224	-7.568$\pm$1.284	-2.780$\pm$1.169
intercept β	5.370$\pm$1.219	6.535$\pm$0.659	5.597$\pm$1.884	3.745$\pm$0.780	5.495$\pm$1.107	3.711$\pm$1.071	4.862$\pm$0.968	7.621$\pm$1.009	3.941$\pm$0.924

Table A4. Best fits for y for the 2+2 outcome with $f(y) = \alpha y + \beta$.

$n \setminus a_0$	1 AU		10 AU		100 AU	
	$a_{\rm s}$ [$e_{\rm min}-e_{\rm max}$]	$a_{\rm l}$ [$e_{\rm min}-e_{\rm max}$]	$a_{\rm s}$ [$e_{\rm min}-e_{\rm max}$]	$a_{\rm l}$ [$e_{\rm min}-e_{\rm max}$]	$a_{\rm s}$ [$e_{\rm min}-e_{\rm max}$]	$a_{\rm l}$ [$e_{\rm min}-e_{\rm max}$]
10 cm^{-3}	1.2990$\pm$0.2193/ [0.0789$-$0.9947]	2.2729$\pm$0.1506 [0.2838$-$0.9970]	1.2965$\pm$0.0994 [0.0634$-$0.9945]	3.1814$\pm$0.1878 [0.1874$-$0.9985]	1.9646$\pm$0.5764 [0.0981$-$0.9973]	2.4125$\pm$0.4754 [0.2318$-$0.9977]
10^2 cm^{-3}	1.5537$\pm$0.3234 [0.1482$-$0.9968]	3.0974$\pm$0.2209 [0.2456$-$0.9979]	1.2965$\pm$0.0994 [0.0000$-$0.9996]	3.3910$\pm$0.3073 [0.0000$-$0.9997]	1.4791$\pm$0.0571 [0.0503$-$0.9969]	3.2876$\pm$0.3606 [0.0923$-$0.9993]
10^3 cm^{-3}	1.2338$\pm$0.3610 [0.1350$-$0.9876]	3.88354$\pm$0.1297 [0.0324$-$0.9998]	1.6341$\pm$0.2023 [0.2400$-$0.9941]	4.2376$\pm$0.2541 [0.3163$-$0.9988]	1.7470$\pm$0.1731 [0.2743$-$0.9991]	2.9867$\pm$0.1820 [0.0693$-$0.9997]

Table A5. Best fits for the eccentricities for each binary for the 2+2 outcome with $f(y) \sim e^{\lambda}$. Maximum and minimum values for e are written below each value of λ.